Phonon transport governed by intrinsic scattering in short-period AlN/GaN superlattices

B. Baer,[1] D. G. Walker,[1] and L. Lindsay[2,*]
[1]*Mechanical Engineering, Vanderbilt University, Nashville, Tennessee 37235, USA*
[2]*Materials Science and Technology Division, Oak Ridge National Laboratory, Oak Ridge, Tennessee 37831, USA*

(Received 25 October 2023; accepted 8 March 2024; published 27 March 2024)

We employ density functional theory based phonon transport methods to provide a rigorous understanding of the nature of thermal transport in coherent short-period AlN/GaN superlattices (SLs), with period lengths up to three unit cells of each, and compare these with properties of their bulk constituents. Increasing the period length leads to phonon band folding with frequency gaps and thus smaller phonon velocities and more phonon scattering than in bulk, both of which reduce lattice thermal conductivity (κ). Contrary to expectations, we find that velocity variations among larger-period AlN/GaN SLs play only a minor role in cross-plane κ reductions, while variations in intrinsic phonon scattering are strongly correlated with their transport behaviors. This work provides insights into the microscopic behaviors of technologically relevant nanostructured materials, which are likely applicable to a wider range of SL systems and other nanostructures.

DOI: 10.1103/PhysRevB.109.104310

I. INTRODUCTION

A remarkable expansion in the breadth (as measured by number of materials) and depth (as measured by physical insights) of numerical characterization and understanding of lattice thermal transport in condensed matter has been recently driven by the advent of density functional theory derived Peierls-Boltzmann transport (DFTPBT) methods [1,2] and open-access codes built from them [3–5]. Some of these calculations have been used to support experimental findings [1] and common expectations linking lattice properties to thermal conductivity (κ) [6], while some have made surprising predictions that challenge these common expectations [7,8]. Regardless, the power of DFTPBT to provide insights into phonon transport behaviors has been impressive.

Some of these works [7,9,10] have demonstrated strong correlations of phonon dispersion features with intrinsic phonon scattering resistance. In particular, calculations have demonstrated that in compound materials with large mass differences between the constituent atoms an energy gap can open between low-frequency heat-carrying acoustic phonons and high-frequency optic phonons [7,9]. This was shown to limit the phase space for phonon-phonon interactions [3,11,12] and to underlie relatively high thermal conductivities in materials such as GaN [9] and BAs [7].

Such analysis has been applied to a variety of crystalline solids with varying dimensionalities; however, less work has been done with regard to complex nanostructured materials such as semiconductor superlattices (SLs) and how this nanostructuring relates to properties of the bulk constituents. SL systems consist of alternating layers of two (or more) semiconductors with tunable thicknesses having commensurate periodicities that give rise to properties significantly different from those in the constituent materials [13–17]. Designing the SL structure enables the optimization of their properties for applications including microelectronics [18], thermoelectrics [19], and optoelectronics [20]. However, these varied applications make conflicting demands on the thermal properties of SLs. For example, a thermoelectric device requires low κ to maintain a temperature gradient, while a light emitting diode requires high κ for heat management. This makes understanding the impact of SL design on κ important.

In this work, we use DFTPBT to critically examine microscopic phonon behaviors and lattice κ for technologically relevant AlN/GaN short-period SLs [from a single (Al/Ga)N wurtzite unit cell (four atoms; $\frac{1}{2}+\frac{1}{2}$ SL) up to alternating three wurtzite layers each of AlN and GaN (24 atoms; 3+3 SL)] and compare with those from bulk AlN and GaN (see Fig. 1 for the structure of the 1+1 SL). Calculations demonstrate monotonically decreasing κ in the cross-plane direction (κ_{cross}) in going from bulk to the SLs with increasing period length. This behavior is correlated with variations in dispersion behaviors (band folding and band flattening via minigaps induced by broken symmetry [14,22,23]). While the interfaces do not explicitly introduce interfacial phonon scattering in our coherent crystals, the increased structural complexity and symmetry breaking leads to decreased phonon velocities and increased intrinsic scattering, and thus lower κ. While the κ_{cross} reductions are not surprising, the calculations here clarify that the key feature governing this behavior is increased intrinsic scattering and detail how this varies from system to system. Section II gives a brief description of the AlN/GaN SL structures and the theoretical and numerical methods used to describe their transport behaviors. Section III presents calculation results and discussions of them, while Section IV provides a brief summary.

II. STRUCTURE AND NUMERICAL METHODS

DFT calculations were implemented with the QUANTUM ESPRESSO (QE) software package [24] using the localized density approximation (LDA) of Perdew and Zunger for the

*lindsaylr@ornl.gov

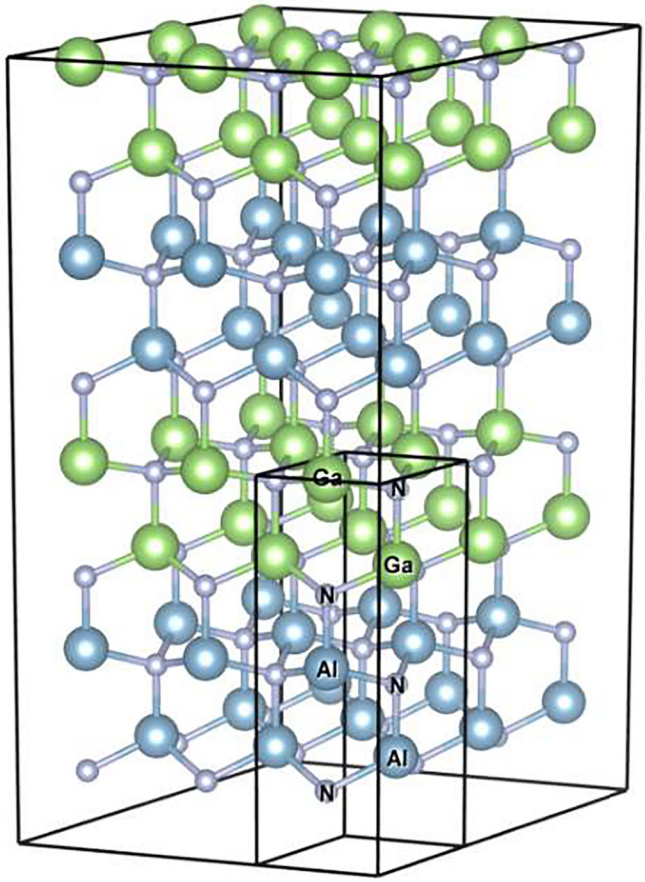

FIG. 1. 1+1 SL structure. A single unit cell is outlined and labeled within. Image produced using VESTA [21].

exchange correlation functionals [25] and projector-augmented wave (PAW) pseudopotentials for the core electrons in each material. The 3*d* electrons for Ga were included in valence.

A. Structure

Bulk wurtzite AlN and GaN were constructed from standard crystallographic positions (hexagonal space group $P6_3mc$) and then relaxed [in-plane a and cross-plane c lattice parameters (see Table I) and an internal degree of freedom u (distance between the anion and cation sublattices)] to minimize the total energy to within 10^{-10} Ry and residual forces to 10^{-6} Ry/bohr using a plane-wave energy cutoff of 100 Ry and a 7×7×5 k-point sampling mesh. $n+n$ SL unit cells were created from the relaxed bulk AlN and GaN systems, by combining n consecutive unit cells of AlN with n consecutive unit cells of GaN along the c direction for 1+1 (eight atoms), 2+2 (16 atoms), and 3+3 (24 atoms) SLs. We also considered the case of replacing one Ga atom in bulk GaN with an Al atom, effectively creating a $\frac{1}{2}+\frac{1}{2}$ SL (four atoms). This SL is particularly useful for bridging comparison of thermal transport properties of bulk with larger SLs because its first Brillouin zone (FBZ) is nominally unchanged when compared with the bulk materials. The SL unit cells were fully relaxed following the same procedure as for the bulk systems, except with reduced k-point sampling in the c direction (7×7×3 for the 1+1 and 2+2 SLs and 7×7×1 for the 3+3 SL) to maintain a roughly constant reciprocal space sampling density. SL structures with an even number of layers of the underlying wurtzite structure have trigonal symmetry, while those with an odd number of layers retain their original hexagonal symmetry [26]. SL calculations here are limited to $n \leqslant 3$ due to the increasing numerical expense of the full microscopic anharmonic transport calculations with increasing number of unit cell atoms.

TABLE I. Lattice parameters, TA and LA low-frequency velocities along the c axis, and in-plane and cross-plane room-temperature thermal conductivities of each material.

	a [c] (Å)	c-axis v_{TA} [v_{LA}] (km/s)	κ_{in} [κ_{cross}] (W/m K)
AlN	3.09 [4.94]	5.9 [11.0]	256 [257]
GaN	3.16 [5.16]	3.9 [8.1]	201 [227]
½+½	3.12 [5.06]	4.6 [9.3]	160 [115]
1+1	3.12 [10.12]	4.6 [9.2]	127 [54]
2+2	3.13 [20.22]	4.6 [9.2]	126 [40]
3+3	3.13 [30.32]	4.6 [9.2]	128 [34]

B. Interatomic force constants and transport

Harmonic and anharmonic interatomic force constants (IFCs) are required to determine vibrational structure (i.e., phonon frequencies $\omega_{\mathbf{q}j}$, and eigenvectors $\varepsilon_{k\alpha}^{\mathbf{q}j}$) and intrinsic scattering rates ($1/\tau_{\mathbf{q}j}$, inverse of phonon lifetimes) that are determined by lowest-order quantum perturbation theory [1,3,11]:

$$\frac{1}{\tau_{\mathbf{q}j}} = \sum_{\mathbf{q}'j'}\sum_{\mathbf{q}''j''} W^{+}_{\mathbf{q}j,\mathbf{q}'j',\mathbf{q}''j''} + W^{-}_{\mathbf{q}j,\mathbf{q}'j',\mathbf{q}''j''}/2, \tag{1}$$

$$W^{\pm}_{\mathbf{q}j,\mathbf{q}'j',\mathbf{q}''j''} = \frac{\pi\hbar}{4N}\frac{|\Psi_{-\mathbf{q}j,\mp\mathbf{q}'j',\mathbf{q}''j''}|^2}{\omega_{\mathbf{q}j}\omega_{\mathbf{q}'j'}\omega_{\mathbf{q}''j''}}(n_{\mathbf{q}j}+1)\left(n_{\mathbf{q}'j'} \pm \frac{1}{2} + \frac{1}{2}\right) \times n_{\mathbf{q}''j''}\delta(\omega_{\mathbf{q}j} \pm \omega_{\mathbf{q}'j'} - \omega_{\mathbf{q}''j''}) \times \delta(\mathbf{q} \pm \mathbf{q}' - \{\mathbf{q}'' + \mathbf{G}\}), \tag{2}$$

$$\Psi_{\mathbf{q}j,\mathbf{q}'j',\mathbf{q}''j''} = \sum_{k,l'k',l''k''}\sum_{\alpha\beta\gamma}\frac{\Phi^{0k,l'k',l''k''}_{\alpha\beta\gamma}}{\sqrt{m_k m_{k'} m_{k''}}}\varepsilon_{k\alpha}^{\mathbf{q}j}\varepsilon_{k'\beta}^{\mathbf{q}'j'}\varepsilon_{k''\gamma}^{\mathbf{q}''j''}e^{i\mathbf{q}'\cdot\mathbf{R}_{l'}}e^{i\mathbf{q}''\cdot\mathbf{R}_{l''}}, \tag{3}$$

all of which feed into thermal conductivity calculations:

$$\kappa_\alpha = \frac{1}{V_0}\sum_{\mathbf{q}j} C_{\mathbf{q}j} v^2_{\mathbf{q}j\alpha}\tau_{\mathbf{q}j}, \tag{4}$$

where $\mathbf{q}$ is the phonon wave vector, j is phonon polarization, the sum is over all polarizations and wave vectors in the FBZ, $v_{\mathbf{q}j\alpha}$ is group velocity in the α Cartesian direction, $C_{\mathbf{q}j}$ is the mode-dependent heat capacity, and V_0 is the unit cell volume. In Eqs. (2) and (3), $\Phi^{0k,l'k',l''k''}_{\alpha\beta\gamma}$ is the third-order derivative of the interatomic potential (anharmonic IFC among three atoms), m_k is the mass of atom k, $\mathbf{R}_l$ is a lattice vector locating the l unit cell, $\mathbf{G}$ is a reciprocal lattice vector, $n_{\mathbf{q}j}$ is the Bose-Einstein distribution, and N is the number of unit cells in the crystal.

Interatomic forces from a PHONO3PY-generated [5] series of supercells with small atomic displacements (0.032 Å) were determined from QE self-consistent electronic structure calculations using Γ-point-only sampling and a plane-wave energy cutoff of 80 Ry. These forces are used to construct harmonic and anharmonic IFCs by numerical differentiation. For harmonic and anharmonic IFC calculations, $4\times4\times Z$ and $3\times3\times Z$ supercells, respectively, were constructed from the relaxed SL unit cells (described above): $Z = 3$ for bulk systems and the $\frac{1}{2}+\frac{1}{2}$ SL, $Z = 2$ for the $1+1$ SL, and $Z = 1$ for the 2+2 and 3+3 SLs. These correspond to systems ranging from 192 to 384 atoms for harmonic calculations and from 108 to 216 atoms for anharmonic calculations. Anharmonic IFCs were calculated using smaller supercells due to their large numerical cost and relatively shorter interaction range (truncated here at 3 Å, smaller than previous calculations on similar systems [9,27]). This short interaction range (though not fully converged) gives reasonable agreement with measured data for the bulk systems and enables fully microscopic calculations for the larger SL systems, which would otherwise be numerically prohibitive. Harmonic IFC calculations included all interactions within the supercell.

To model the longitudinal-transverse optical (LO-TO) phonon splitting in these polar compounds, density functional perturbation theory (DFPT) calculations were performed using QE to obtain the Born charges and high-frequency dielectric tensors required for constructing nonanalytical corrections to the dynamical matrices arising from long-range Coulomb interactions [28]. For this, self-consistent electronic calculations were performed using a plane-wave energy cutoff of 80 Ry and Brillouin zone sampling with a k-point grid of $7\times7\times Z$, with $Z = 5$ for the bulk systems, the $\frac{1}{2}+\frac{1}{2}$ SL, and the 1+1 SL, $Z = 3$ for the 2+2 SL, and $Z = 1$ for the 3+3 SL. The DFPT calculations were performed with Γ-point-only sampling. Harmonic IFC files, QE structural input files, Born charges, and dielectric tensors for each system are provided in the Supplemental Material [29].

The above-described IFCs are inputs to PHONO3PY calculations of thermal conductivity tensors for which there are two relevant elements in our SL systems: in-plane thermal conductivity (κ_{in}) and cross-plane thermal conductivity (κ_{cross}). These were calculated within the relaxation time approximation (RTA)—thus no directional dependence to the lifetimes in Eq. (4)—with a $10\times10\times10$ reciprocal space sampling mesh for all systems considered. (A $20\times20\times20$ sampling mesh for determining κ of AlN gave negligible difference.) We employ even grids that effectively oversample the c axis in our anisotropic materials as we are most interested in transport along this axis. For bulk AlN and GaN the full solutions of the DFTPBT give κ values <6% larger than those from the RTA, though at a significantly larger computational cost. As the SLs have generally stronger phonon scattering, we expect the discrepancy between RTA and full calculations to be negligible. Phonon-isotope scattering due to natural isotopic mass disorder was included via quantum perturbation theory [30]. We did not consider the role of four-phonon interactions as these are predicted to be relatively unimportant in determining GaN thermal conductivity around room temperature and below [31].

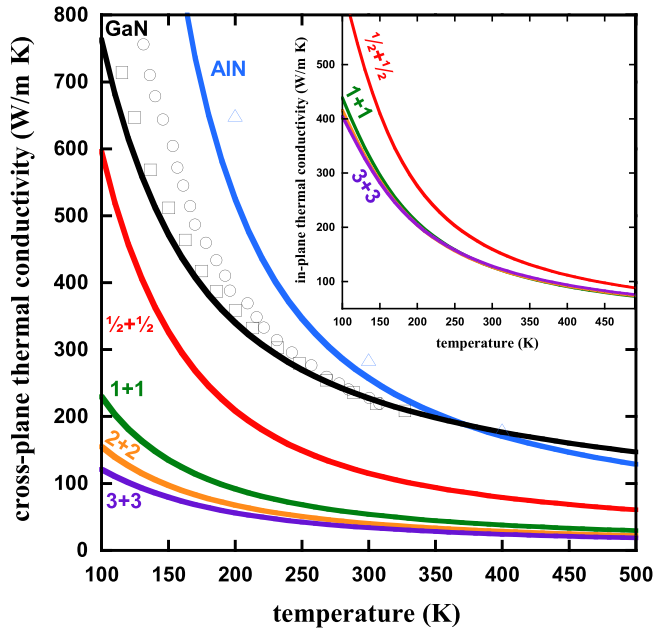

FIG. 2. Temperature-dependent cross-plane thermal conductivities of AlN (blue), GaN (black), $\frac{1}{2}+\frac{1}{2}$ SL (red), 1+1 SL (green), 2+2 SL (orange), and 3+3 SL (purple)—curves for calculations; symbols for measurements: black circles [32], black squares [33], and blue triangles [34]. The inset gives the temperature-dependent in-plane thermal conductivities of the SL systems.

III. RESULTS

Here we present calculated κ values and underlying properties to support a critical analysis of the coherent microscopic mechanisms governing intrinsic thermal transport in bulk and AlN/GaN SL systems. We begin with general remarks of the transport behaviors of the SL and bulk materials, then build microscopic comparisons of the bulk and SL systems based on how band folding underlies the variations in phonon velocities and scattering rates that govern κ.

Calculated temperature-dependent thermal conductivities of the $\frac{1}{2}+\frac{1}{2}$, 1+1, 2+2, and 3+3 SL structures are given in Fig. 2 and compared with those of the component bulk materials (see Table I for in-plane and cross-plane room-temperature κ values for each system). The thermal conductivities of bulk AlN and GaN have been well studied, both experimentally and theoretically [9,32–35], while AlN/GaN SLs have received less attention, particularly short-period SLs [36–39]. Measured κ data for the bulk materials are included in Fig. 2, while measured data for short-period SLs are not available. Calculated κ_{in} are not sensitive to SL structuring for systems beyond the $\frac{1}{2}+\frac{1}{2}$ SL (inset to Fig. 2). On the other hand, κ_{cross} values of the SL systems are lower than those of the bulk and decrease monotonically from the shortest-period SL ($\frac{1}{2}+\frac{1}{2}$) to the largest-period SL (3+3) over the entire temperature range considered. Previous calculations have demonstrated this behavior in other short-period SLs [14,15,40] and have shown a minimum in κ with SL period due to a crossover in going from a wavelike conduction regime at short periods (as seen here) to a particlelike conduction regime at long periods (where mean free paths of the phonon

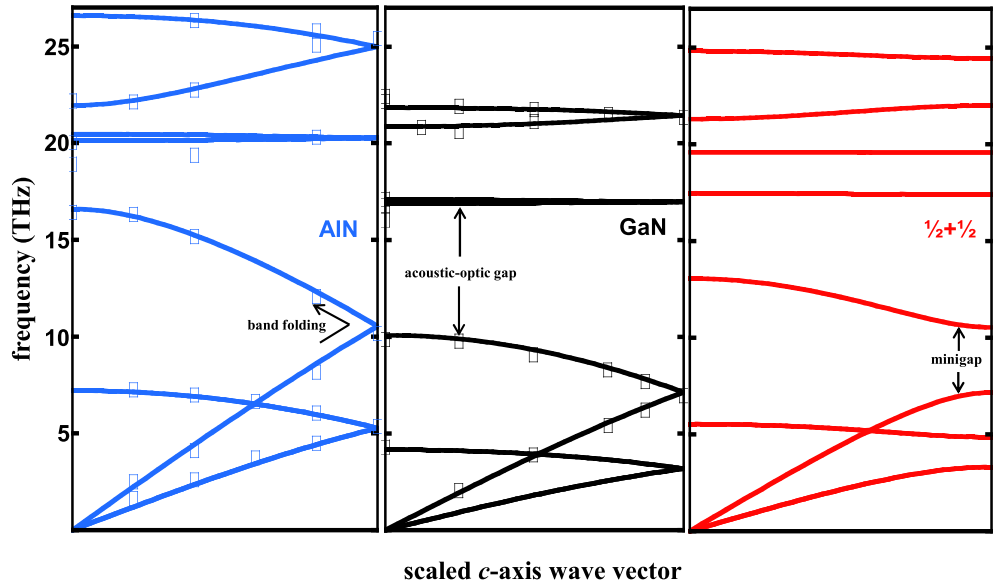

FIG. 3. Cross-plane phonon dispersions for AlN (left), GaN (middle), and the $\frac{1}{2}+\frac{1}{2}$ SL (right). Note that each system has band folding in this direction. For bulk, this arises due to the internal symmetry of the formula units within the wurtzite unit cell. Black squares [43] (GaN) and blue squares [44] (AlN) are measured data from inelastic x-ray scattering.

heat carriers tend to be smaller than the interfacial spacings). Most experiments have reported increasing κ with SL period (particlelike conduction regime) due to decreasing interfacial densities and thus less scattering of phonon heat carriers with decreasing number of interfaces [36,37,39]. However, coherent low-frequency acoustic phonon transport was reported for low-temperature measurements in layered GaAs/AlAs SL systems [16]. Naively, one might expect the κ of the $\frac{1}{2}+\frac{1}{2}$ SL to lie between those of AlN and GaN as may be expected using a virtual crystal approximation (VCA; averaging properties of the bulk members) in isoelectronic materials, similar to that done in calculations for alloys [41,42]. However, this approximation neglects interfacial effects on the phonon dispersions. Similarly, VCA alloy calculations also require adding phonon-mass-defect scattering to give expected reduced κ values.

A. Phonon-isotope scattering

Previous work demonstrated that phonon-isotope scattering is important in GaN partly because intrinsic phonon-phonon scattering is relatively weak (further discussions below) and partly due to Ga having a large natural isotope mixture (60.1% ^{69}Ga and 39.9% ^{71}Ga) [9]. On the other hand, natural Al is isotopically pure so phonon-isotope scattering is very weak in AlN (N atoms are nearly isotopically pure: 99.6% ^{14}N and 0.4% ^{15}N). At lower temperatures phonon-isotope scattering becomes more important as resistive phonon-phonon scattering gets frozen out. The extra mass-defect scattering in GaN leads to lower κ in GaN than in AlN with decreasing temperature. Weaker phonon-isotope scattering in AlN translates, to a degree, into the SL systems, which have half the Ga concentration of GaN and thus reduced phonon-isotope interactions, though they have more intrinsic scattering from the additional structural complexity. Both combine to make the SL systems rather insensitive to phonon-isotope interactions: $<$10% reduction in κ at room temperature.

B. Band folding

All bulk and SL systems have band folding along the high-symmetry c axis (see Fig. 3 for the bulk and $\frac{1}{2}+\frac{1}{2}$ SL systems). Bulk AlN and GaN bands have a single band fold arising from the internal symmetry of the formula units within the wurtzite unit cell (2_1 screw axis) [45]. The 1+1, 2+2, and 3+3 SLs have increased band folding, and correspondingly smaller FBZs, commensurate with their increasing layer numbers [14,22,23]. One primary difference between the bulk and SL systems (besides the number of folded bands) is the opening of minigaps at the zone boundary (for all SL systems) and zone center (for the 1+1, 2+2, and 3+3 SLs). In the bulk systems, symmetry of the 2_1 screw axis mandates that the folded bands at the zone boundary are degenerate and have equal and opposite velocities [45]. The degeneracies are broken in the SL systems and each folded band has zero velocity at the zone boundaries and zone center. This gapping coupled with zero velocities at the zone boundary and zone center are important as they tend to reduce the overall phonon velocities along the c axis and can ease restrictions on conservation of energy and momentum conditions for enhanced intrinsic scattering, both of which give reduced κ_{cross}.

C. Velocities

As fast phonons can carry heat more efficiently than slower phonons, group velocities along varying directions are critical to determining κ and κ anisotropy. Here we discuss the role of phonon group velocities and their variations in determining the κ behaviors of the SL systems.

As demonstrated in Table I, the SL systems are anisotropic, having significantly higher κ_{in} than κ_{cross}. Within the RTA

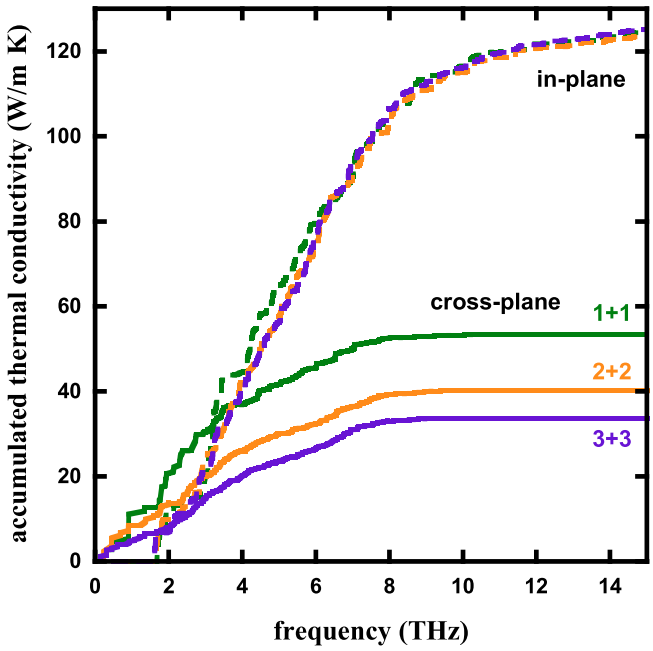

FIG. 4. Room-temperature thermal conductivity accumulations with frequency for the 1+1 SL (green curves), the 2+2 SL (orange curves), and the 3+3 SL (purple curves). Dashed curves correspond to in-plane κ_{acc}, while solid curves correspond to cross-plane κ_{acc}.

used here, the directional dependence for a given system derives solely from the phonon group velocities. To examine this more closely, Fig. 4 gives the room-temperature thermal conductivity accumulations (κ_{acc}) with frequency for the 1+1, 2+2, and 3+3 SL systems, both in-plane and cross-plane. The in-plane κ_{acc} curves overlap for the three SL materials over most of the frequency range. The 1+1 SL cross-plane κ_{acc} curve is highest, followed by the 2+2 SL and then the 3+3 SL curves over most of the frequency range. For each SL, the low-frequency region (<3 THz) has higher cross-plane group velocities than in-plane, as demonstrated by the cross-plane curves being higher than their in-plane counterparts. Above $\sim$ 3 THz this behavior reverses and the in-plane velocities dominate, thus leading to higher in-plane κ_{acc} curves in this frequency region and overall higher κ_{in}.

To better understand the decreasing κ_{cross} behavior with SL period and how band folding and velocity variations propagate into this, we correlate the *c*-axis velocities of TA phonons and their associated folded bands [Fig. 5 (top) (GaN and $\frac{1}{2}+\frac{1}{2}$ SL) and Fig. 6 (top) (GaN, 1+1 SL, and 3+3 SL)] with their estimated contributions to room-temperature cross-plane κ_{acc} [Fig. 5 (bottom) and Fig. 6 (bottom)]. Table I gives the low-frequency TA and LA velocities along the *c* axis for each material. The TA phonon contributions to κ are estimated by correlating the *c*-axis dispersions with the FBZ frequencies from the transport calculations to reasonably detangle TA modes and their folded counterparts from the other polarizations, i.e., folded LA branches. The SL systems have generally higher frequency dispersions (thus higher-velocity acoustic phonons and blueshifted optic branches) than those of GaN because their overall masses are smaller due to replacing half of the Ga atoms with Al. This higher velocity is seen in

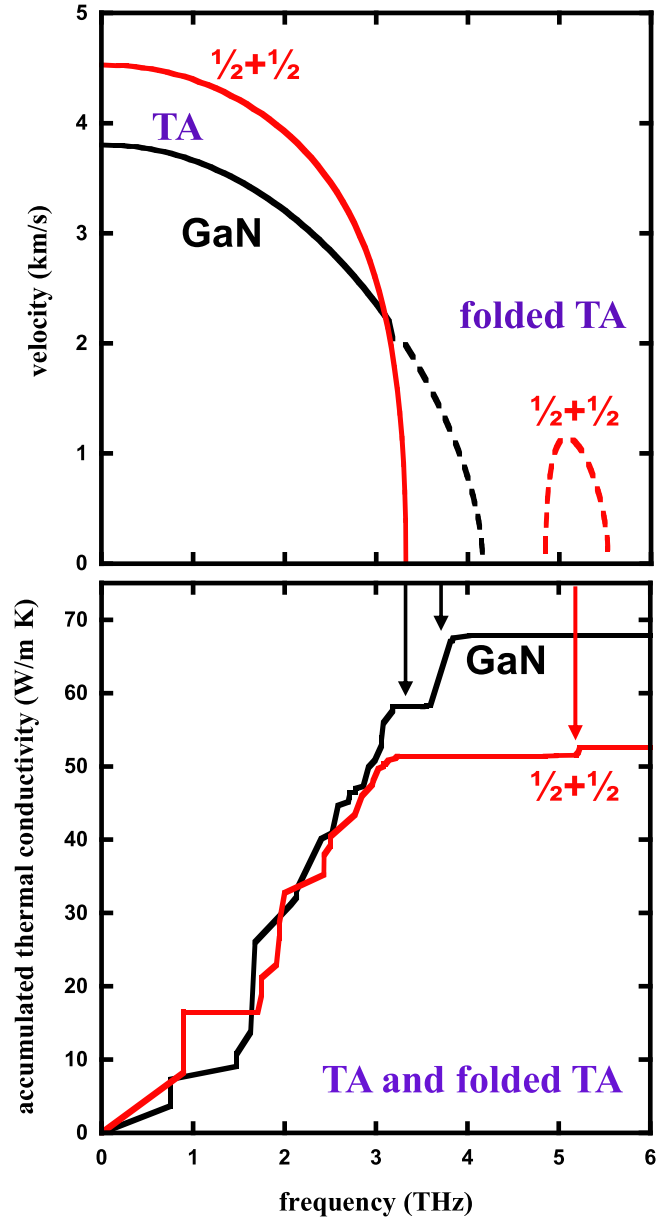

FIG. 5. (Top) Absolute values of cross-plane group velocities of TA phonons (solid curves) and associated folded bands (dashed curves) as a function of frequency for bulk GaN (black) and the $\frac{1}{2}+\frac{1}{2}$ SL (red). (Bottom) Corresponding room-temperature cross-plane thermal conductivity accumulations with frequency for the TA phonons (and associated folded bands). Arrows highlight the correspondence between features in the velocities and the κ_{acc}.

Figs. 5 (top) and 6 (top) for low-frequency TA phonons and in Table I. Despite the $\frac{1}{2}+\frac{1}{2}$ SL having significantly higher-velocity TA modes below 3 THz, the associated cross-plane κ_{acc} is similar to that of GaN. This counterintuitive finding is our first hint that variations in intrinsic phonon scattering behaviors (discussed below) are the driving mechanism for differences in κ among the bulk and SL systems. The folded TA modes $\sim$3.5 THz in GaN reach velocities about twice as high as the folded modes, $\sim$5.25 THz of the $\frac{1}{2}+\frac{1}{2}$ SL. In GaN these contribute $\sim$10 W/m K, while in the $\frac{1}{2}+\frac{1}{2}$ SL

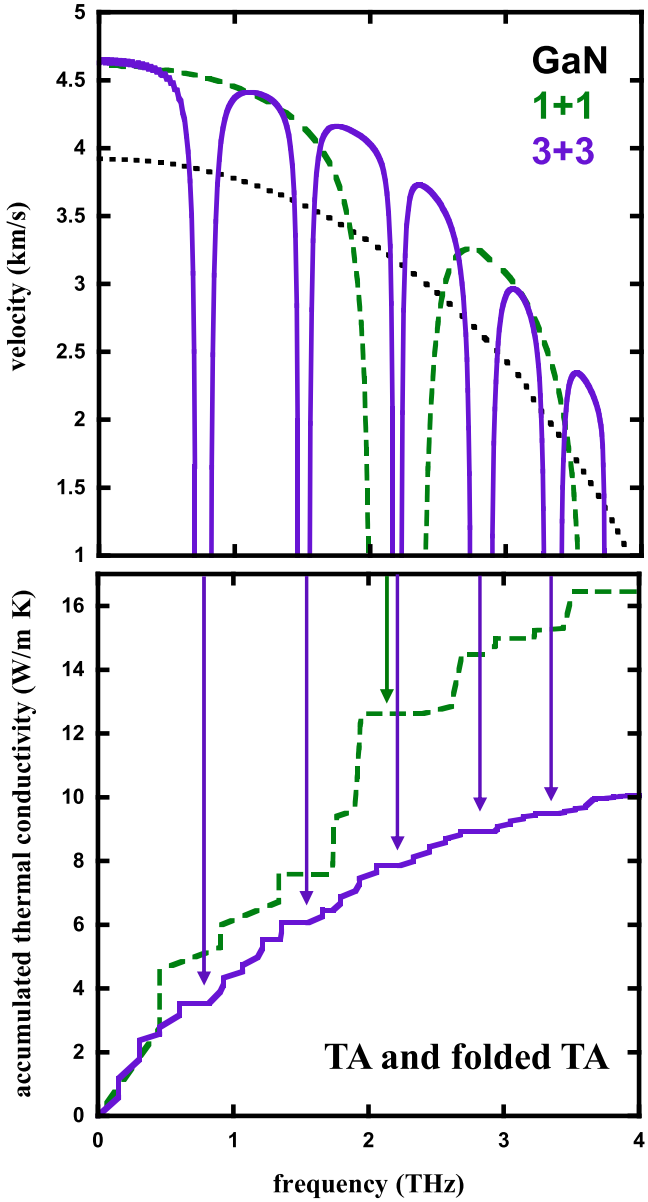

FIG. 6. (Top) Absolute values of group velocities of TA phonons (and associated folded bands) as a function of frequency for bulk GaN (black dotted curve), the 1+1 SL (green dashed curves), and the 3+3 SL (purple solid curves). (Bottom) Corresponding room-temperature cross-plane thermal conductivity accumulations with frequency for the TA phonons (and associated folded bands). Arrows highlight the correspondence between disappearing velocities and reduced thermal conductivity contributions.

they contribute ~ 1 W/m K [see Fig. 5 (bottom)]. The lower contributions from the flatter $\frac{1}{2}+\frac{1}{2}$ SL folded band are not surprising; however, the order of magnitude difference also suggests that increased scattering is playing a comparative role as the reduced velocities in determining κ for the folded bands.

With increasing SL period, the minigaps become smaller and smaller, as one might expect in the limit that the system becomes bulklike (i.e., half bulk GaN interfaced with half bulk AlN). For example, the lowest folded TA (LA) branches have frequency gaps going from 1.53 THz (3.37 THz) in the $\frac{1}{2}+\frac{1}{2}$ SL to 0.41 THz (1.12 THz) in the 1+1 SL to 0.18 THz (0.56 THz) in the 2+2 SL to 0.12 THz (0.39 THz) in the 3+3 SL. Thus as SL periods become large the portions of frequency space with reduced velocities, though more numerous, cover less range. Figure 6 (top) compares the velocities for the TA branches and corresponding folded branches of the 1+1 and 3+3 SLs with those of bulk GaN and corresponding cross-plane κ_{acc} [Fig. 6 (bottom)]. The minigaps and reduced velocities in the SL systems can also be correlated with lower κ_{acc} contributions. Note that sparse FBZ sampling, particularly at low frequencies, can also mimic flat portions of κ_{acc} in frequency space due to finite discretization of FBZ numerical integrations [46]. Like the $\frac{1}{2}+\frac{1}{2}$ SL, the 1+1 and 3+3 SLs have many TA and folded modes with velocities larger than those of GaN [see Fig. 6 (top)], with $\sim 20\%$ of frequency space along the c axis (and thus number of modes) having lower velocities or minigaps with no modes at all. Despite 80% of the SL modes in frequency space having higher velocities than GaN along the c axis, the total TA contributions to κ_{cross} of the 1+1 and 3+3 SLs are ~ 4 and ~ 7 times smaller, respectively, than that of GaN.

D. Intrinsic phonon scattering

Given the discrepancies in understanding SL κ behaviors in terms of phonon velocities alone, we now reexamine the thermal conductivity calculations in the context of phonon-phonon scattering.

Going back to the bulk systems, a rather counterintuitive result is κ_{cross} values of AlN and GaN are similar at high temperatures despite AlN having little phonon-isotope scattering and a smaller average mass with higher-velocity acoustic phonons (see dispersions in Fig. 3). This can be understood in terms of larger acoustic phonon lifetimes in GaN, particularly in the frequency window 5–8 THz [see Fig. 7 (top)], which is correlated with a large increase in the room-temperature cross-plane κ_{acc} of GaN in the same frequency region [Fig. 7 (bottom)]. AlN and GaN have similar κ_{acc} up to ~ 5 THz despite slower phonons in GaN and from 8–15 THz AlN has further contributions from dispersive modes at higher frequencies than GaN because Al atoms are lighter than Ga atoms.

As seen in Eqs. (1)–(3), lifetimes are a complex interplay of anharmonic IFCs, frequencies, masses, eigenvectors, distributions, and phase factors. Masses enter inversely into the scattering rates, but also tend to reduce the overall frequencies of each system, which also enter Eq. (2) inversely. Thus, correlating increased lifetimes with increased mass in GaN compared to the other systems is not straightforward. However, if variations in masses were the leading driver for scattering rate differences, then we would expect these differences to be larger, across the entire frequency spectrum, and the heavier $\frac{1}{2}+\frac{1}{2}$ SL should have larger lifetimes than AlN, which is not evident in Fig. 7 (top).

Variations in the anharmonic IFCs are not expected to be the governing difference in the phonon lifetimes among the bulk and SL systems as Al and Ga are isoelectronic. To demonstrate this, Table II gives the inequivalent, nonzero

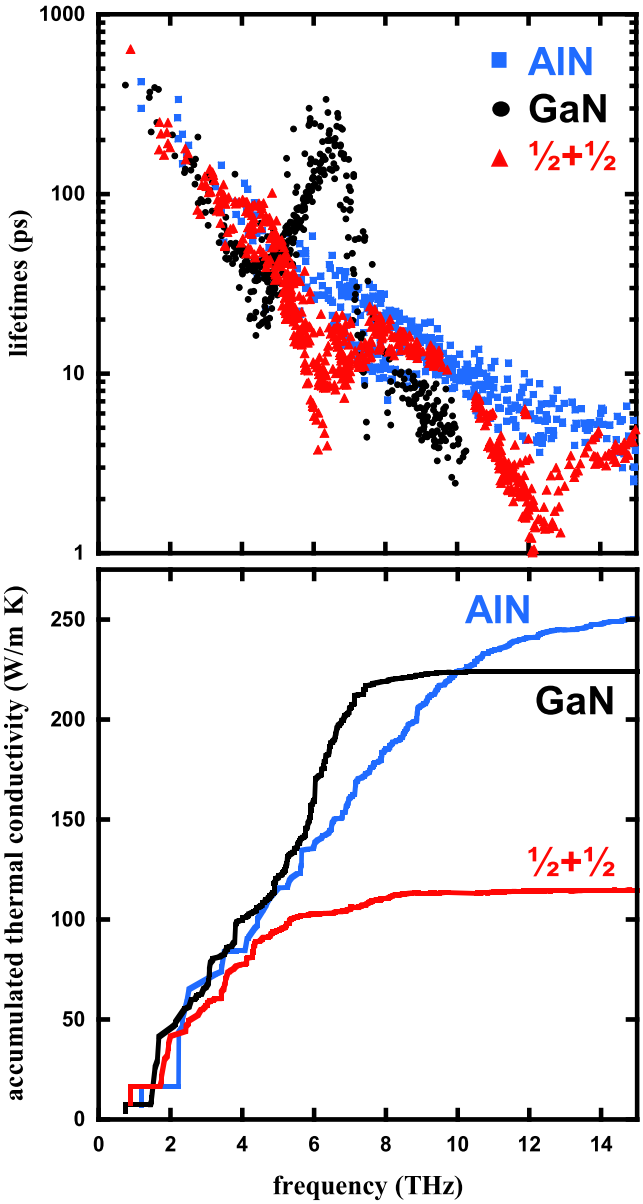

FIG. 7. (Top) Room-temperature phonon lifetimes for AlN (blue squares), GaN (black circles), and the $\frac{1}{2}+\frac{1}{2}$ SL (red triangles). (Bottom) Corresponding cross-plane thermal conductivity accumulations.

third-order anharmonic IFCs for the self-interaction matrix ($\Phi^{lk,lk,lk}_{\alpha\beta\gamma} = \Phi^{k}_{\alpha\beta\gamma}$) for each atom type ($k$ = Al, Ga, or N) in each system. These anharmonic IFCs generally have the largest magnitudes. The 1+1, 2+2, and 3+3 SLs have more than one inequivalent atom for each atom type; thus value ranges are given. The Al IFCs in AlN are similar to the Ga IFCs in GaN, and so too are the IFCs for the N atoms in each system. Also, corresponding IFCs across all the systems are similar.

As discussed in previous work, the kinematic constraints of energy and momentum conservation can play significant roles in determining phonon lifetimes [7,9–12]. This can be measured by the scattering phase space for each phonon mode

TABLE II. Nonzero, self-interaction anharmonic IFCs ($\Phi^{lk,lk,lk}_{\alpha\beta\gamma} = \Phi^{k}_{\alpha\beta\gamma}$ in eV/Å^3) for different atom types k = Al, Ga, or N in each system. The 1+1, 2+2, and 3+3 SLs have more than one inequivalent atom for each atom type; thus value ranges are given. Same with the N atoms in the $\frac{1}{2}+\frac{1}{2}$ SL.

	AlN	GaN	$\frac{1}{2}+\frac{1}{2}$	1+1	2+2	3+3
Φ^{Al}_{xxz}	33.7	–	31.7	31.1–31.6	31.0–31.5	31.0
Φ^{Al}_{xxy}	52.3	–	48.6	47.4–48.7	47.6–48.8	47.5–48.8
Φ^{Al}_{zzz}	70.6	–	72.1	71.5–72.2	71.0–72.0	71.2–71.9
Φ^{Ga}_{xxz}	–	32.9	35.3	35.3–35.4	35.3–35.5	35.3–35.5
Φ^{Ga}_{xxy}	–	48.2	50.9	51.2–52.3	51.2–52.6	51.3–52.6
Φ^{Ga}_{zzz}	–	65.6	64.0	63.5–65.0	63.2–64.8	63.3–64.8
Φ^{N}_{xxz}	34.9	35.0	31.7–39.0	31.6–39.0	31.5–38.9	31.5–38.9
Φ^{N}_{xxy}	54.5	50.9	51.2–53.2	50.0–54.9	49.8–55.3	49.8–55.3
Φ^{N}_{zzz}	70.7	68.7	65.4–72.4	65.2–72.2	65.1–73.3	65.0–72.2

given by

$$P_{\mathbf{q}j} = \sum_{\mathbf{q}'j'}\sum_{\mathbf{q}''j''}\delta(\omega_{\mathbf{q}j}+\omega_{\mathbf{q}'j'}-\omega_{\mathbf{q}''j''})\delta(\mathbf{q}+\mathbf{q}'-\{\mathbf{q}''+\mathbf{G}\}) + \frac{1}{2}\delta(\omega_{\mathbf{q}j}-\omega_{\mathbf{q}'j'}-\omega_{\mathbf{q}''j''})\delta(\mathbf{q}-\mathbf{q}'-\{\mathbf{q}''+\mathbf{G}\}). \quad (5)$$

The mode-dependent phase space for AlN and GaN are compared with their corresponding scattering rates (inverse lifetimes) in Fig. 8. The phase space dips for GaN directly coincide with the dips in the GaN scattering rates. Note that scattering rates generally decrease with decreasing frequency due to translational invariance built into Eq. (3). Both AlN and GaN have some degree of bunching of the acoustic branches (small spacing between TA and LA branches), which was shown to limit all-acoustic three-phonon scattering and thus give increased acoustic phonon lifetimes [7]. However, GaN has a significantly larger frequency gap ($\sim$ 4 THz) between the acoustic and optic phonons than that of AlN ($\sim$ 1.5 THz), which is driven by the larger mass difference between the constituent atoms of GaN (Ga : N $\sim$ 4.98) over that of AlN (Al : N $\sim$ 1.93). Thus, energy conservation limits the phase space available for two acoustic phonons to interact with an optic phonon in GaN [9], which drives κ to be higher than otherwise expected.

Comparing again the calculations for bulk GaN with the $\frac{1}{2}+\frac{1}{2}$ SL, the SL system has higher overall acoustic velocities [see Fig. 5 (top)]; this alone should lead to higher κ_{cross} in the $\frac{1}{2}+\frac{1}{2}$ SL. However, the minigap opening and the folded LA branch in the $\frac{1}{2}+\frac{1}{2}$ SL acts like a new optic mode in the otherwise acoustic-optic frequency gap of GaN. This midgap LA folded branch opens the phase space for scattering of the heat-carrying acoustic phonons, particularly in the 5–8 THz range where the lifetimes of the $\frac{1}{2}+\frac{1}{2}$ SL dip significantly, exactly where the GaN lifetimes peak [see Fig. 7 (top)]. Unlike κ_{acc} of GaN, the $\frac{1}{2}+\frac{1}{2}$ SL κ_{acc} is predominantly flat in this frequency range and higher [see Fig. 7 (bottom)]. To further verify the origin of the increased scattering, Fig. 9 shows mode-dependent scattering rates and phase spaces for bulk GaN compared to an approximate model built from the bulk GaN harmonic and anharmonic IFCs, but with vary-

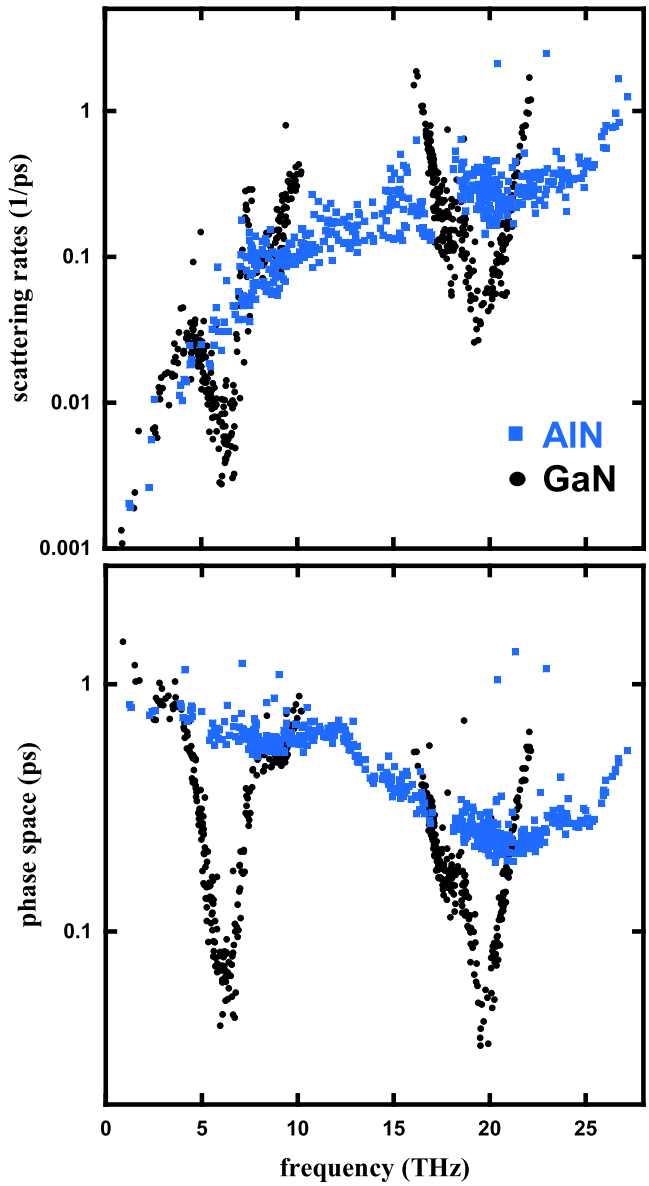

FIG. 8. (Top) Calculated room-temperature scattering rates for GaN (black circles) and AlN (blue squares). (Bottom) Corresponding calculated mode-dependent phase spaces for each material. Note that these calculations used harmonic and anharmonic IFCs as in Refs. [9] and [47].

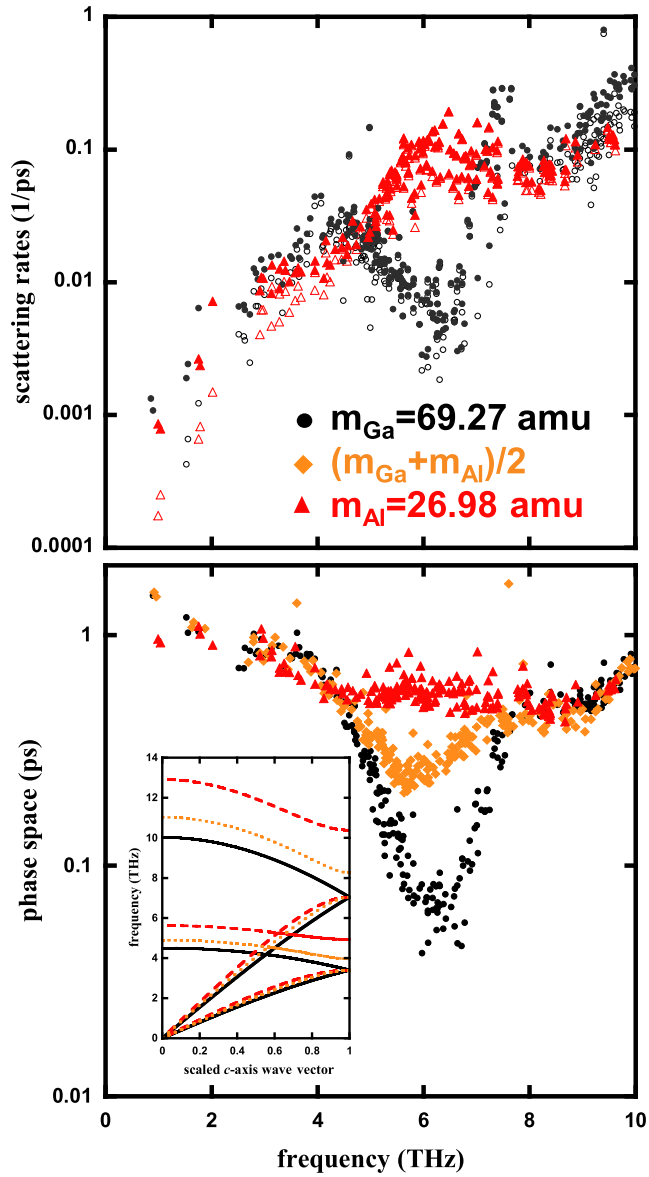

FIG. 9. Room-temperature scattering rates (top) and mode-dependent phase spaces (bottom) for a toy model built from the harmonic and anharmonic IFCs of GaN with one Ga mass varied: 69.72 amu (Ga mass; black circles), 48.35 amu (average of Ga and Al masses; orange diamonds), and 26.98 amu (Al mass; red triangles). The inset gives the low-frequency c-axis phonon dispersion for each system. For the scattering rates (top), hollow symbols correspond to rates that involve at least one folded LA mode (7–15 THz range) and filled symbols correspond to the total rates. Note that these calculations used harmonic and anharmonic IFCs as in Ref. [9].

ing mass of one of the Ga atoms: 69.72 amu (Ga mass), 48.35 amu (average of Ga and Al masses), and 26.98 amu (Al mass). Although approximate, this toy model enables the isolation of mass effects in determining transport trends. As the mass decreases, the TA and LA branches remain largely unchanged, while the folded branches become gapped and lift to higher frequencies [inset to Fig. 9 (bottom]. As these folded bands lift to higher frequencies, the phase space increases in the 5–8 THz range [Fig. 9 (bottom)]. Figure 9 (top) shows the corresponding overall scattering rates (filled symbols) for GaN and the toy $\frac{1}{2}+\frac{1}{2}$ model with Al mass compared with those that involve at least one of the folded LA modes in the 7–15 THz range (hollow symbols). This demonstrates that in this frequency range the scattering with the folded LA modes dominates the behavior, particularly for the $\frac{1}{2}+\frac{1}{2}$ SL. A direct phase space comparison for the larger SLs cannot be made as they have different degrees of freedom, i.e., more branches that both scatter phonons and carry heat. Furthermore, as the SL period becomes larger and coupling between the GaN and AlN becomes limited to a small interfacial region, matrix element symmetries [Eq. (3)] are expected to also play an important role (discussion below).

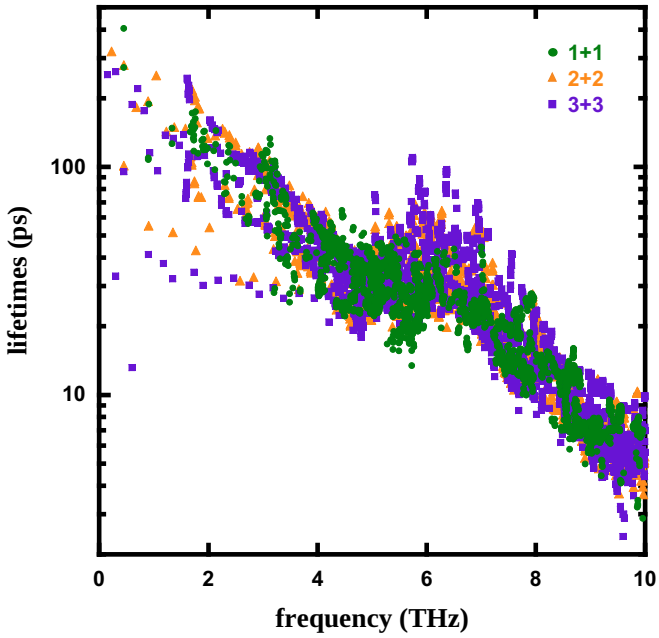

FIG. 10. Room-temperature phonon lifetimes for the 1+1 SL (green circles), the 2+2 SL (orange triangles), and the 3+3 SL (purple squares).

The larger-period SLs have generally smaller lifetimes than the $\frac{1}{2} + \frac{1}{2}$ SL below 5 THz [compare Figs. 7 (top) and 10] and thus have correspondingly suppressed κ values (see Table I). Variations among the κ_{cross} of the 1+1, 2+2, and 3+3 SLs can also be correlated with lifetime variations in this frequency region. Figure 11 (left) gives the mode contributions to room-temperature κ_{cross} as a function of the magnitude of the cross-plane component of the group velocity (v_{cross}) for modes with frequency less than 10 THz and $v_{\text{cross}} > 1$ km/s in the 1+1 and 3+3 SLs. These modes account for $\sim 95\%$ of the total κ_{cross} in each system. Both systems demonstrate increasing κ contributions with increasing velocity, generally following the expected square dependence trend. For the higher-velocity modes, the 1+1 SL has significantly higher mode κ than the 3+3 system due to having larger lifetimes. To demonstrate this, lifetime values (in picoseconds) are labeled for select modes. These modes are also correlated with sharp increases in the cross-plane κ_{acc} of the 1+1 SL that underlie the difference between the cross-plane κ values of the 1+1 and 3+3 SLs (see Fig. 11 (right)).

Interestingly, in the 5–8 THz region for the larger SLs the phonon lifetimes have a peak, similar to that found in GaN though smaller, and this peak increases with period length from the 1+1 SL to the 2+2 SL to the 3+3 SL. Branch folding in SLs can ease phase space restrictions for intrinsic phonon scattering as folded branches fill more frequency space and energy conservation is easier to attain. However, this is not the full story as similar calculations can be performed in supercells with repeated units along the c axis for bulk materials, effectively mimicking the SL unit cells. In this case, the bulk systems would have similar band folding (though without the minigaps) and presumably increased phase space for scattering similar to the larger-period SLs, but should have the same calculated κ. This arises as internal symmetries within the large bulk supercells lead to quantum phase interference that manifests in conservation conditions for matrix elements

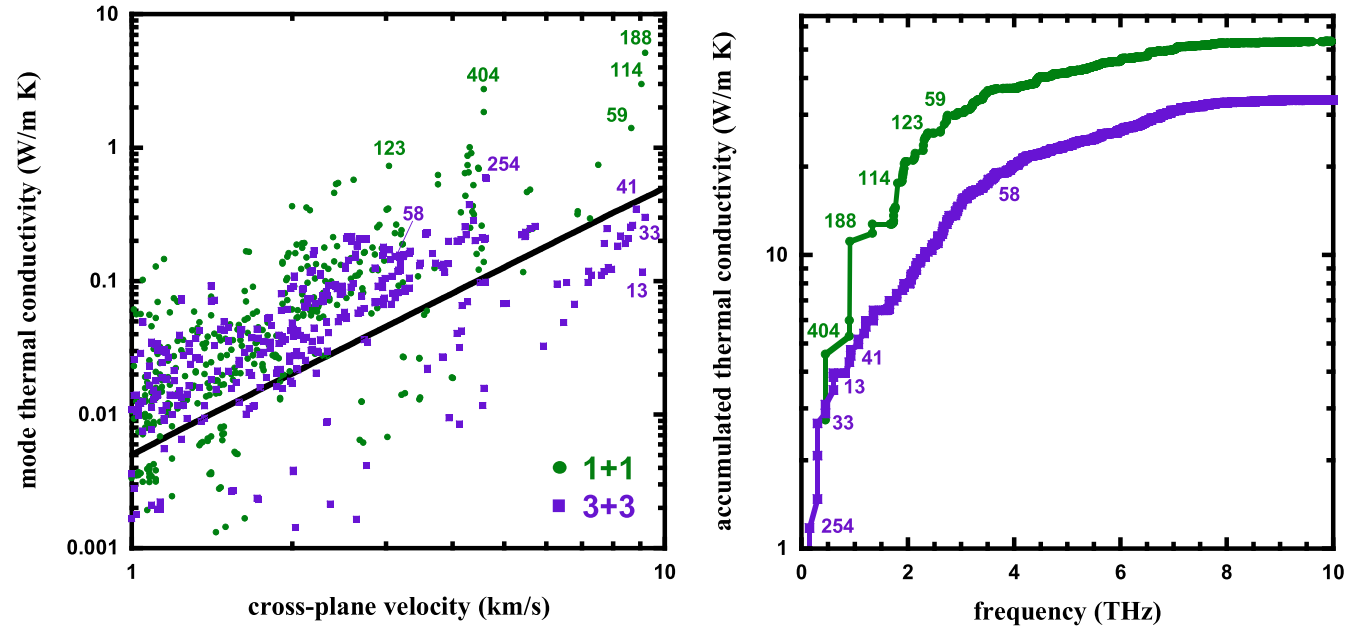

FIG. 11. (Left) Mode contributions to room-temperature κ versus magnitude of cross-plane velocity component (v_{cross}) for the 1+1 SL (green circles) and the 3+3 SL (purple squares). Only modes with frequencies less than ~10 THz with $v_{\text{cross}} > 1$ km/s are shown; these sum up to ~95% of the total κ. Numbers label the lifetimes in picoseconds for select modes that give relatively large κ contributions. The black line highlights the square dependence of the mode κ on velocity. (Right) Room-temperature cross-plane thermal conductivity accumulation versus frequency for the 1+1 SL (green circles and curve) and the 3+3 SL (purple squares and curve). Numbers give the lifetimes for select modes corresponding to the left figure.

connecting the various bands. That is, for three phonons to interact, they must come from particular phonon branches. This was demonstrated recently for systems with internal translational symmetries in their conventional unit cells [48]. In the real SL systems, symmetry is broken and thus such phase interference conditions do not exist and scattering is allowed. However, with increasing SL period perhaps such symmetries approximate those of bulk supercells and hence approximate bulk scattering behavior. This may explain the growing lifetime peak found in Fig. 10 with increasing SL period. Unfortunately, pushing calculations beyond the 3+3 SL to test this is currently beyond our numerical resources.

While we cannot be certain without similarly rigorous calculations, we suspect generally similar dispersion and transport behaviors in short-period SLs comprising other two-component semiconducting systems. Band folding is governed simply by the SL periodicity and the gapping of these bands is likely predominantly governed by the mass differences between the constituent layers [see inset to Fig. 9 (bottom)], as most semiconducting SLs in the literature are composed of isoelectronic elements. Furthermore, closing of these gaps is not material specific, but arises due to approaching the limit of two bulk materials with a small interfacial region. κ reductions in other SL materials from band folding and increased scattering phase space will depend on the intrinsic bulk scatterings. If the intrinsic scattering is strong, as in complex or strongly anharmonic materials, then κ reductions with SL layering will be relatively smaller compared to those in materials with weak intrinsic scattering.

IV. SUMMARY

Using calculations of phonon dispersions and intrinsic scattering rates based on density functional theory and quantum perturbative methods, we developed rigorous insights into the phonon transport behaviors of coherent short-period AlN/GaN superlattices and their bulk constituents. We correlated features of their dispersions (band folding with frequency gap openings) with variations in phonon velocities and scattering rates, both of which govern lattice thermal conductivity. Surprisingly, we demonstrate that decreased velocities from flattened folded bands only play a minor role in reducing κ of larger-period AlN/GaN SL systems. Rather, changes in scattering rates were more strongly correlated with the variations in κ behaviors in different frequency regions of the bulk and SL systems. This work provides a rigorous description of the underlying mechanisms that govern phonon transport in technologically relevant AlN/GaN SL systems and may be applicable to a wider variety of SLs and nanostructures.

ACKNOWLEDGMENTS

Calculations and development of the paper were supported by the U.S. Department of Energy, Office of Science, Office of Basic Energy Sciences, Material Sciences and Engineering Division. B.B. and D.G.W. were supported in part by the National Renewable Energy Lab (Contract No. DE-FOA-0002252 CPS Agreement No. 38213). The calculations used resources of the Compute and Data Environment for Science (CADES) at the Oak Ridge National Laboratory, which is supported by the Office of Science of the U.S. Department of Energy under Contract No. DE-AC05-00OR22725, and resources of the National Energy Research Scientific Computing Center, which is supported by the Office of Science of the U.S. Department of Energy under Contract No. DE-AC02-05CH11231. This work was conducted in part using the resources of the Advanced Computing Center for Research and Education at Vanderbilt University, Nashville, TN. We thank Xiaolong Yang, Tianli Feng, and Xiulin Ruan for providing four-phonon scattering rates for GaN.

[1] D. A. Broido, M. Malorny, G. Birner, N. Mingo, and D. A. Stewart, Intrinsic lattice thermal conductivity of semiconductors from first principles, Appl. Phys. Lett. **91**, 231922 (2007).

[2] T. Ma, P. Chakraborty, X. Guo, L. Cao, and Y. Wang, First-principles modeling of thermal transport in materials: Achievements, opportunities, and challenges, Int. J. Thermophys. **41**, 1 (2020).

[3] W. Li, J. Carrete, N. A. Katcho, and N. Mingo, ShengBTE: A solver of the Boltzmann transport equation for phonons, Comput. Phys. Commun. **185**, 1747 (2014).

[4] T. Tadano, Y. Gohda, and S. Tsuneyuki, Anharmonic force constants extracted from first-principles molecular dynamics: Applications to heat transfer simulations, J. Phys.: Condens. Matter **26**, 225402 (2014).

[5] A. Togo, L. Chaput, and I. Tanaka, Distributions of phonon lifetimes in Brillouin zones, Phys. Rev. B **91**, 094306 (2015).

[6] G. A. Slack, Nonmetallic crystals with high thermal conductivity, J. Phys. Chem. Solids **34**, 321 (1973).

[7] L. Lindsay, D. A. Broido, and T. L. Reinecke, First-principles determination of ultrahigh thermal conductivity of boron arsenide: A competitor for diamond?, Phys. Rev. Lett. **111**, 025901 (2013).

[8] M. Simoncelli, N. Marzari, and F. Mauri, Unified theory of thermal transport in crystals and glasses, Nat. Phys. **15**, 809 (2019).

[9] L. Lindsay, D. A. Broido, and T. L. Reinecke, Thermal conductivity and large isotope effect in GaN from first principles, Phys. Rev. Lett. **109**, 095901 (2012).

[10] N. K. Ravichandran and D. Broido, Phonon-phonon interactions in strongly bonded solids: Selection rules and higher-order processes, Phys. Rev. X **10**, 021063 (2020).

[11] J. M. Ziman, *Electrons and Phonons* (Oxford University Press, London, 1960).

[12] L. Lindsay and D. A. Broido, Three-phonon phase space and lattice thermal conductivity in semiconductors, J. Phys.: Condens. Matter **20**, 165209 (2008).

[13] A. P. Silin, A review of topical problems: Semiconductor superlattices, Sov. Phys. Usp. **28**, 972 (1985).

[14] G. Mahan, Thermal conductivity of superlattices, in *Thermal Conductivity* (Springer, Boston, 2004), Chap. 1.6, pp. 153–165.

[15] D. A. Broido and T. L. Reinecke, Effect of superlattice structure on the thermoelectric figure of merit, Phys. Rev. B **51**, 13797 (1995).

[16] M. N. Luckyanova, J. Garg, K. Esfarjani, A. Jandl, M. T. Bulsara, A. J. Schmidt, A. J. Minnich, S. Chen, M. S. Dresselhaus, Z. Ren, E. A. Fitzgerald, and G. Chen, Coherent phonon heat conduction in superlattices, Science **338**, 936 (2012).

[17] A. Bulusu and D. G. Walker, Quantum modeling of thermoelectric performance of strained Si/Ge/Si superlattices using nonequilibrium Green's function method, J. Appl. Phys. **102**, 073713 (2007).

[18] A. Krishna, A. Raj, N. Hatui, S. Keller, and U. K. Mishra, Investigation of nitrogen polar *p*-type doped GaN/$Al_xGa_{(1-x)}N$ superlattices for applications in wide-bandgap *p*-type field effect transistors, Appl. Phys. Lett. **115**, 172105 (2019).

[19] L. W. Whitlow and T. Hirano, Superlattice applications to thermoelectricity, J. Appl. Phys. **78**, 5460 (1995).

[20] Y. Y. Zhang and Y. A. Yin, Performance enhancement of blue light-emitting diodes with a special designed AlGaN/GaN superlattice electron-blocking layer, Appl. Phys. Lett. **99**, 221103 (2011).

[21] K. Momma and F. Izumi, VESTA 3 for three-dimensional visualization of crystal, volumetric and morphology data, J. Appl. Cryst. **44**, 1272 (2011).

[22] M. V. Simkin and G. D. Mahan, Minimum thermal conductivity of superlattices, Phys. Rev. Lett. **84**, 927 (2000).

[23] D. A. Broido and T. L. Reinecke, Lattice thermal conductivity of superlattice structures, Phys. Rev. B **70**, 081310(R) (2004).

[24] P. Giannozzi, S. Baroni, N. Bonini, M. Calandra, R. Car, C. Cavazzoni, D. Ceresoli, G. L. Chiarotti, M. Cococcioni, I. Dabo, A. D. Corso, S. Gironcoli, S. Fabris, G. Fratesi, R. Gebauer, U. Gerstmann, C. Gougoussis, A. Kokalj, M. Lazzeri, L. Martin-Samos *et al.*, QUANTUM ESPRESSO: A modular and open-source software project for quantum simulations of materials, J. Phys.: Condens. Matter **21**, 395502 (2009).

[25] J. P. Perdew and A. Zunger, Self-interaction correction to density-functional approximations for many-electron systems, Phys. Rev. B **23**, 5048 (1981).

[26] Y. E. Kitaev, M. F. Limonov, P. Tronc, and G. N. Yushin, Raman-active modes in wurtzite $(GaN)_m(AlN)_n$ superlattices, Phys. Rev. B **57**, 14209 (1998).

[27] N. H. Protik, A. Katre, L. Lindsay, J. Carrete, N. Mingo, and D. Broido, Phonon thermal transport in 2H, 4H, and 6H silicon carbide from first principles, Mater. Today Phys. **1** (June), 31 (2017).

[28] P. Giannozzi, S. de Gironcoli, P. Pavone, and S. Baroni, *Ab initio* calculation of phonon dispersions in semiconductors, Phys. Rev. B **43**, 7231 (1991).

[29] See Supplemental Material at http://link.aps.org/supplemental/10.1103/PhysRevB.109.104310 for harmonic IFC files, QE structural input files, Born charges, and dielectric tensors for each system.

[30] S.-i. Tamura, Isotope scattering of large-wave-vector phonons in GaAs and InSb: Deformation-dipole and overlap-shell models, Phys. Rev. B **30**, 849 (1984).

[31] X. Yang, T. Feng, J. Li, and X. Ruan, Stronger role of four-phonon scattering than three-phonon scattering in thermal conductivity of III-V semiconductors at room temperature, Phys. Rev. B **100**, 245203 (2019).

[32] A. Jeżowski, P. Stachowiak, T. Plackowski, T. Suski, S. Krukowski, M. Boćkowski, I. Grzegory, B. Danilchenko, and T. Paszkiewicz, Thermal conductivity of GaN crystals grown by high pressure method, Phys. Status Solidi B **240**, 447 (2003).

[33] G. A. Slack, L. J. Schowalter, D. Morelli, and J. A. Freitas, Some effects of oxygen impurities on AlN and GaN, J. Cryst. Growth **246**, 287 (2002).

[34] G. A. Slack, R. A. Tanzilli, R. O. Pohl, and J. W. Vandersande, The intrinsic thermal conductivity of AlN, J. Phys. Chem. Solids **48**, 641 (1987).

[35] A. V. Inyushkin, A. N. Taldenkov, D. A. Chemodubov, E. N. Mokhov, S. S. Nagalyuk, V. G. Ralchenko, and A. A. Khomich, On the thermal conductivity of single crystal AlN, J. Appl. Phys. **127**, 205109 (2020).

[36] A. Filatova-Zalewska, Z. Litwicki, K. Moszak, W. Olszewski, K. Opołczyńska, D. Pucicki, J. Serafińczuk, D. Hommel, and A. Jeżowski, Anisotropic thermal conductivity of AlGaN/GaN superlattices, Nanotechnology **32**, 075707 (2021).

[37] A. Spindlberger, D. Kysylychyn, L. Thumfart, R. Adhikari, A. Rastelli, and A. Bonanni, Cross-plane thermal conductivity of GaN/AlN superlattices, Appl. Phys. Lett. **118**, 062105 (2021).

[38] A. Filatova-Zalewska, Z. Litwicki, and A. Jeżowski, Calculation of thermal conductivity of AlGaN/GaN superlattices, Phys. Status Solidi B **260**, 2200528 (2023).

[39] Y. K. Koh, Y. Cao, D. G. Cahill, and D. Jena, Heat-transport mechanisms in superlattices, Adv. Funct. Mater. **19**, 610 (2009).

[40] A. Ward and D. A. Broido, Intrinsic lattice thermal conductivity of Si/Ge and GaAs/AlAs superlattices, Phys. Rev. B **77**, 245328 (2008).

[41] B. Abeles, Lattice thermal conductivity of disordered semiconductor alloys at high temperatures, Phys. Rev. **131**, 1906 (1963).

[42] J. Garg, N. Bonini, B. Kozinsky, and N. Marzari, Role of disorder and anharmonicity in the thermal conductivity of silicon-germanium alloys: A first-principles study, Phys. Rev. Lett. **106**, 045901 (2011).

[43] T. Ruf, J. Serrano, M. Cardona, P. Pavone, M. Pabst, M. Krisch, M. D'Astuto, T. Suski, I. Grzegory, and M. Leszczynski, Phonon dispersion curves in wurtzite-structure GaN determined by inelastic x-ray scattering, Phys. Rev. Lett. **86**, 906 (2001).

[44] M. Schwoerer-Böhning, A. T. Macrander, M. Pabst, and P. Pavone, Phonons in wurtzite aluminum nitride, Phys. Status Solidi B **215**, 177 (1999).

[45] R. Juneja, X. Li, S. Thébaud, D. H. Moseley, Y. Q. Cheng, M. E. Manley, R. P. Hermann, and L. Lindsay, Phonons in complex twisted crystals: Angular momenta, interactions, and topology, Phys. Rev. B **106**, 094310 (2022).

[46] R. Hanus, R. Gurunathan, L. Lindsay, M. T. Agne, J. Shi, S. Graham, and G. J. Snyder, Thermal transport in defective and disordered materials, Appl. Phys. Rev. **8**, 031311 (2021).

[47] L. Lindsay, D. A. Broido, and T. L. Reinecke, *Ab initio* thermal transport in compound semiconductors, Phys. Rev. B **87**, 165201 (2013).

[48] X. Li, S. Thébaud, and L. Lindsay, Primitive to conventional geometry projection for efficient phonon transport calculations, npj Comput. Mater. **9**, 193 (2023).